Electronic Supplementary Material (ESI) for Journal of Materials Chemistry C.

Supplementary information(S1)

Unexpected p-type thermoelectric transport arising from magnetic Mn substitution in $Fe_2V_{1-x}Mn_xAl$ Heusler compounds

Rajveer Jha[1], Naohito Tsujii[1,*], Fabian Garmroudi[2], Sergii Khmelevskyi[3], Ernst Bauer[2], and Takao Mori[1,4,*]

[1]Research Center for Materials Nanoarchitectonics (MANA), Nanomaterials Field, National Institute for Materials Science (NIMS), 1-2-1 Sengen, Tsukuba 305-0047, Japan

[2]Institute of Solid State Physics, TU Wien, A-1040 Vienna, Austria

[3]Vienna Scientific Cluster Research Center, TU Wien, A-1040 Vienna, Austria

[4]Graduate School of Pure and Applied Sciences, University of Tsukuba, Tennodai 1-1-1, Tsukuba 305-8671, Japan

Fig. S1. (a) XRD patterns for $Fe_2V_{1-x}Mn_xAl$, with the zoomed view of 111-peak at around 27°. (b) XRD patterns for $Fe_2V_{0.9}Mn_{0.1}Al_{1+y}$ with the zoomed view of 111-peak at around 27°.

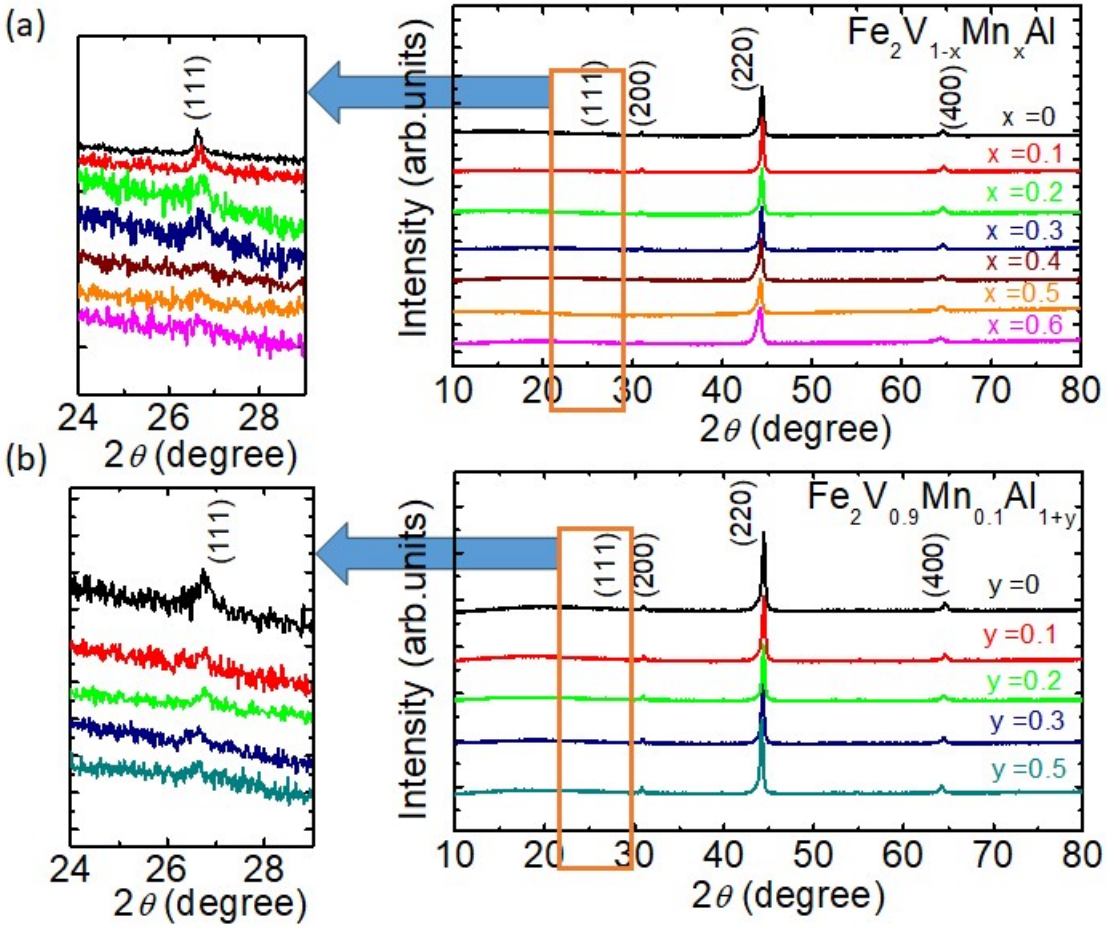

Table S1. Refined structural parameters of Mn-doped $Fe_2V_{1-x}Mn_xAl$ as determined from Rietveld refinement of cubic crystal structure in the space group Fm-3m (No. 225) using XRD data.

Atoms sites labels	Occupancy	Positions		
		x	y	z
Fe	**1**	**0.25**	**0.25**	**0.25**
V/Mn	**1**	**0.5**	**0.5**	**0.5**
Al	**1**	**0**	**0**	**0**

Table S2. The results of Rietveld refinement of $Fe_2V_{1-x}Mn_xAl$.

Samples	Lattice Parameter	Rwp	Re	S	GOF
x	*a* (Å)	(%)	(%)	(%)	
0	5.758(2)	1.229	0.756	1.625	2.641
0.1	5.762(1)	1.095	0.791	1.3845	1.916
0.2	5.764(2)	1.093	0.784	1.3943	1.944
0.3	5.767(1)	1.128	0.772	1.4615	2.130
0.4	5.771(3)	1.249	0.713	1.7517	3.060
0.5	5.774(1)	1.176	0.865	1.3587	1.840
0.6	5.774(2)	1.069	0.829	1.2890	1.660

Table S3. The results of Rietveld refinement of $Fe_2V_{0.9}Mn_{0.1}Al_{1+y}$.

Samples	Lattice Parameter	Rwp	Re	S	GOF
y	*a* (Å)	(%)	(%)	(%)	
0	5.762(1)	1.095	0.791	1.3845	1.916
0.1	5.763(2)	1.079	0.752	1.4359	2.060
0.2	5.764(1)	1.036	0.250	4.1368	17.11
0.3	5.767(2)	1.062	0.263	4.0332	16.26
0.5	5.781(2)	1.094	0.261	4.1933	17.58

Fig.S2. Rietveld refined XRD pattern for the $Fe_2V_{1-x}Mn_xAl$.

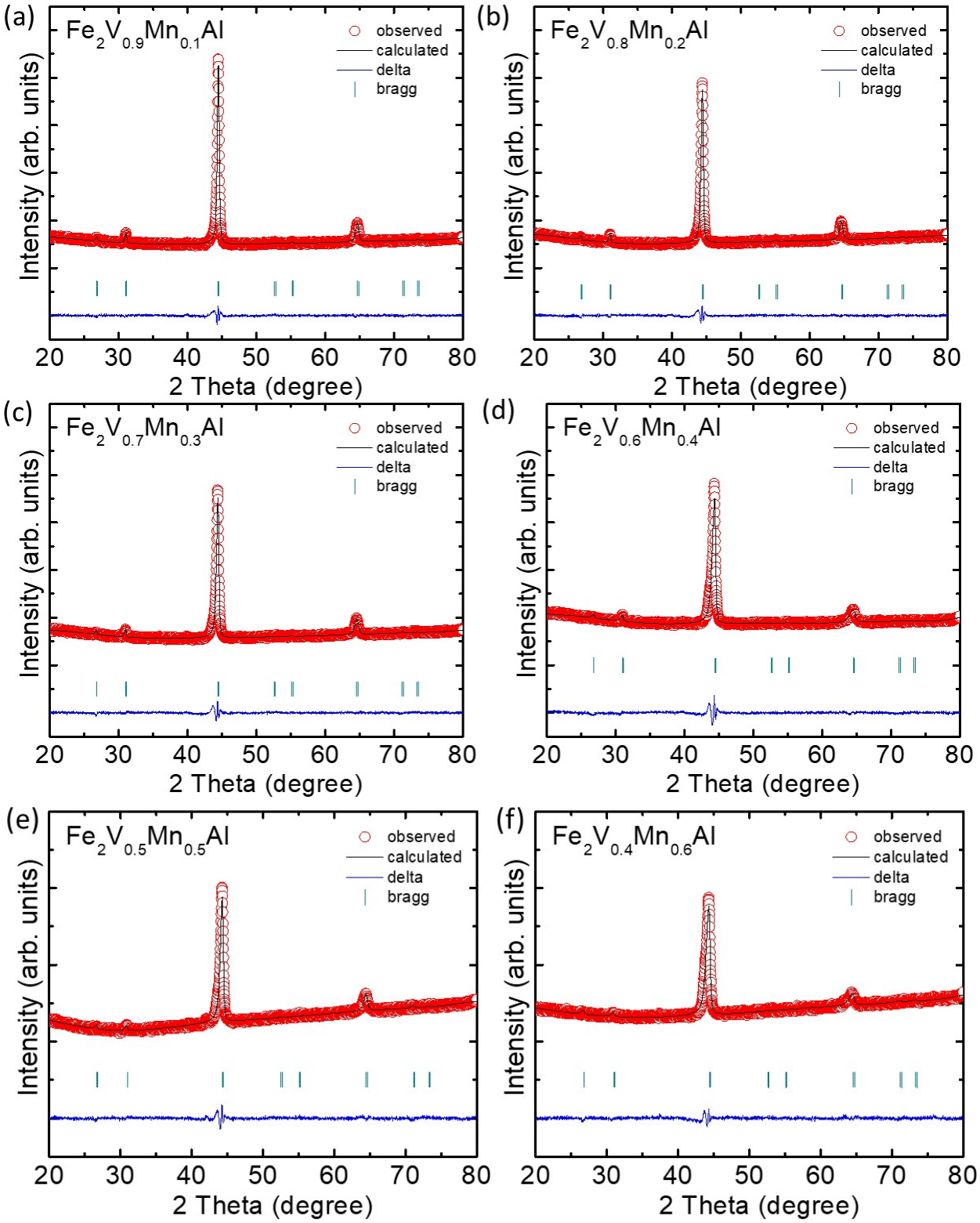

Fig.S3. Rietveld refined XRD pattern for $Fe_2V_{0.9}Mn_{0.1}Al_{1+y}$.

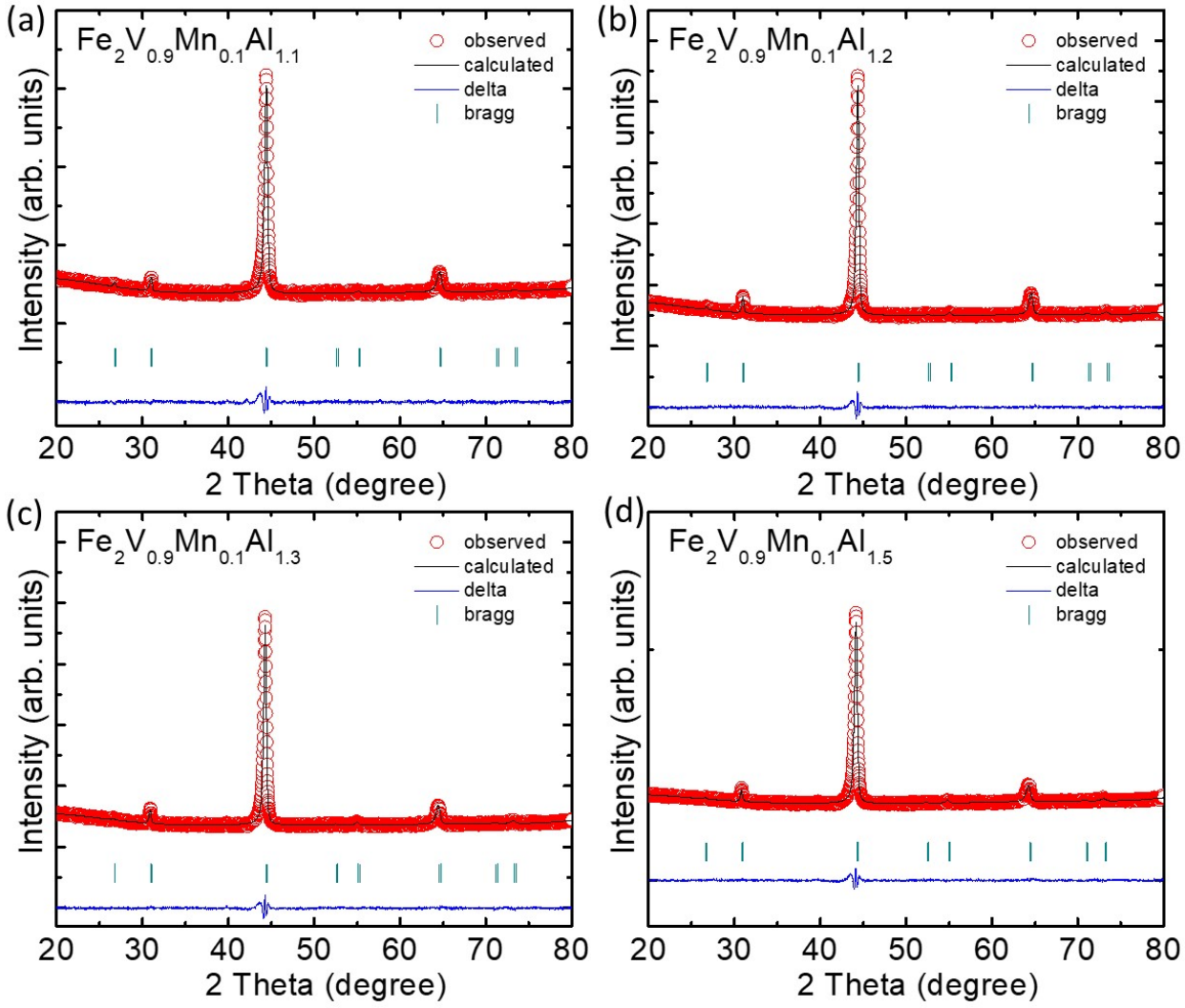

Table S4. Composition analysis of $Fe_2V_{1-x}Mn_xAl$ and $Fe_2V_{0.9}Mn_{0.1}Al_{1+y}$ by SEM + EDS, where the selected area for EDS analysis is about 70 × 70 μm².

Sample	Fe	V	Mn	Al
Nominal	50	25-x	x	25
Fe_2VAl	51.2	23.63	0	25.17
$Fe_2V_{0.9}Mn_{0.1}Al$	51.8	23.64	1.73	23.6
$Fe_2V_{0.8}Mn_{0.2}Al$	50.46	20.67	2.92	25.95
$Fe_2V_{0.7}Mn_{0.3}Al$	50.65	19.8	5.99	23.56
$Fe_2V_{0.6}Mn_{0.4}Al$	52.12	13.11	8.20	26.58
$Fe_2V_{0.5}Mn_{0.5}Al$	52.79	11.69	10.88	24.64
$Fe_2V_{0.4}Mn_{0.6}Al$	50.95	10.32	12.23	26.5
$Fe_2V_{0.9}Mn_{0.1}Al_{1.1}$	51.9	17.95	1.43	28.72
$Fe_2V_{0.9}Mn_{0.1}Al_{1.2}$	49.53	17.36	1.21	31.9
$Fe_2V_{0.9}Mn_{0.1}Al_{1.3}$	49.35	19.1	1.3	30.25
$Fe_2V_{0.9}Mn_{0.1}Al_{1.5}$	46.86	20.7	1.31	31.12

Table S5. The Hall mobility μ_H and Seebeck effective mass (m_s^*/m^*) of $Fe_2V_{1-x}Mn_xAl$ and $Fe_2V_{0.9}Mn_{0.1}Al_{1+y}$ were estimated using the Hall effect and Seebeck coefficient.

Sample	$\mu_H(10^{-4}m^2V^{-1}S^{-1})$	m_s^*/m^*
Fe_2VAl	4.40	---
$Fe_2V_{0.9}Mn_{0.1}Al$	8.46	7.15
$Fe_2V_{0.8}Mn_{0.2}Al$	4.26	11.39
$Fe_2V_{0.7}Mn_{0.3}Al$	3.98	15.65
$Fe_2V_{0.6}Mn_{0.4}Al$	2.82	19.54
$Fe_2V_{0.5}Mn_{0.5}Al$	2.22	40.66
$Fe_2V_{0.4}Mn_{0.6}Al$	1.56	---
$Fe_2V_{0.9}Mn_{0.1}Al_{1.1}$	8.18	10.12
$Fe_2V_{0.9}Mn_{0.1}Al_{1.2}$	6.44	12.29
$Fe_2V_{0.9}Mn_{0.1}Al_{1.3}$	4.38	30.80
$Fe_2V_{0.9}Mn_{0.1}Al_{1.5}$	7.36	10.32

Figure S4 shows the Scanning Electron Microscopy (SEM) and Energy Dispersive Spectroscopy (EDS) measurements to examine the morphology and the chemical composition of the selected $Fe_2V_{0.9}Mn_{0.1}Al_{1.1}$ sample. Figure S4(b-e) shows EDS elemental mapping obtained from the top view of the $Fe_2V_{0.9}Mn_{0.1}Al_{1.1}$ sample. The results suggest a uniform distribution of all elements over the observed area. Two black spots indicate that aluminum oxide is present in the main phase, which is minor and does not affect the thermoelectric properties of the compound. EDS data taken for all the samples suggest that our samples are slightly off-stoichiometric, as is seen in Table S1.

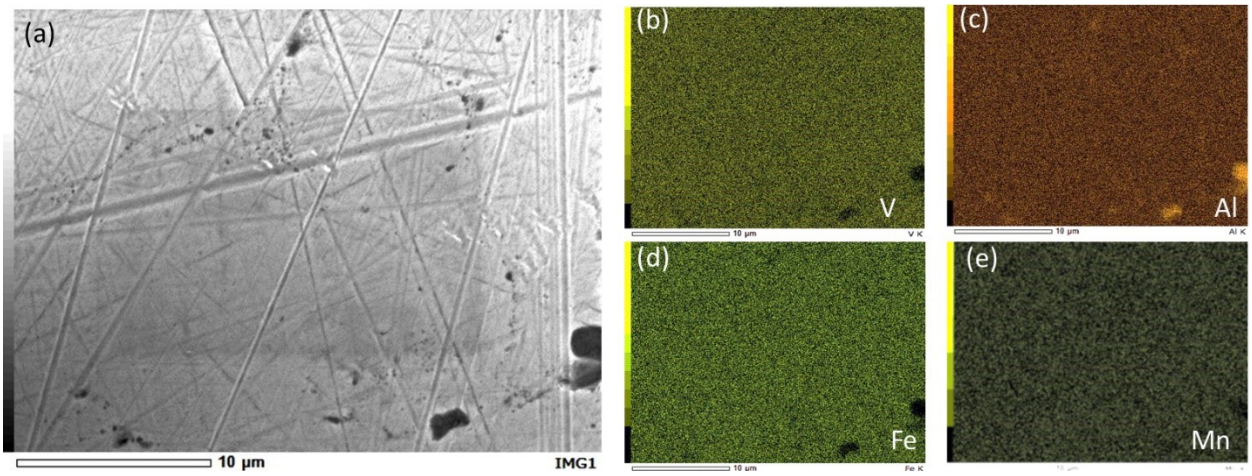

Fig.S4. (a) SEM image of the polished surface and (b-e) the corresponding EDS elemental mapping for the $Fe_2V_{0.9}Mn_{0.1}Al_{1.1}$ sample.

The magnetic properties of Al-rich $Fe_2V_{0.9}Mn_{0.1}Al_{1+y}$ ($y = 0, 0.1, 0.3, 0.5$) samples as shown in Fig. S5(a). All the measured samples show Curie-Weiss behavior. The fitting of H/M vs. temperature curves, measured at B = 1 T for y = 0, 0.1, 0.3, 0.5, is shown in Fig. S5(b). The evaluated magnetic moments μ_{eff} are summarized in Table. 2. Obviously, the effective magnetic moment monotonically decreases with increasing Al concentration in $Fe_2V_{0.9}Mn_{0.1}Al_{1+y}$. Like in the case of $Fe_2V_{1-x}Mn_xAl$, the paramagnetic Curie temperature dramatically changes from ferromagnetic-type interactions for y = 0 ($\theta \sim 50$ K) to substantially large antiferromagnetic correlations for y = 0.5 ($\theta \sim -161$ K). Since there is no apparent peak in the derivative of the

magnetization with respect to temperature, it seems that magnetic ordering is absent for these Al-rich samples. However, there is a small anomaly for the samples with y = 0.5 around T = 70 K, which we attribute to small impurities of Fe or Mn.

Isothermal field-dependent magnetization curves for $Fe_2V_{0.9}Mn_{0.1}Al_{1+y}$ (y = 0, 0.1, 0.3, 0.5) are shown in Fig. S5(c, d) at temperatures 2 K and 300 K, respectively. The absolute values of the magnetization at T = 300 K decrease monotonically with increasing Al concentration in $Fe_2V_{0.9}Mn_{0.1}Al_{1+y}$. In addition, the magnetization curves reveal typical paramagnetic field dependencies, where the slight deviation from linearity refers to the presence of finite magnetic interactions. Compared to the superparamagnetic-like saturating behavior for y = 0 at T = 2 K, the remaining samples show much smaller magnetization. Earlier, magnetic properties for magnetic ions doping in Fe_2VAl and off-stoichiometric Fe_2VAl have been investigated extensively.

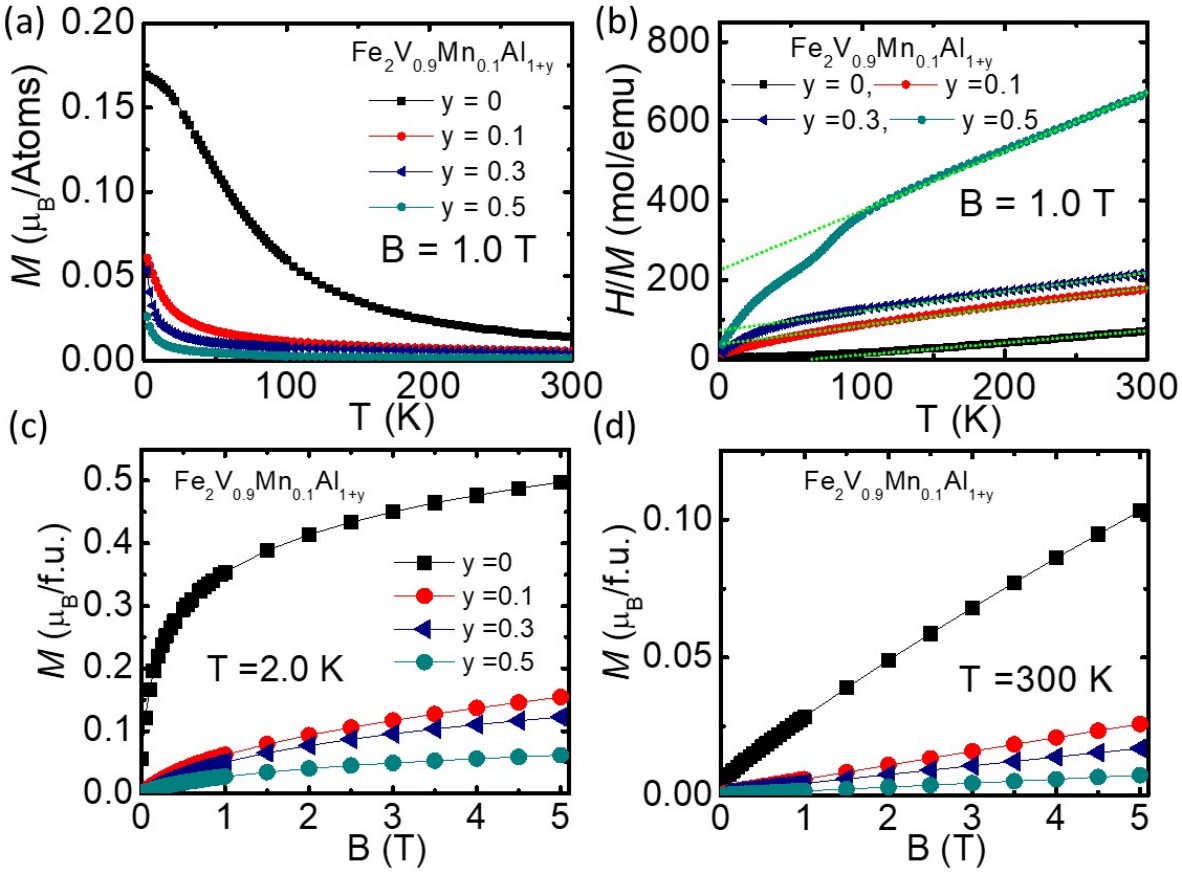

Fig.S5. (a) The temperature dependence of magnetization M for $Fe_2V_{0.9}Mn_{0.1}Al_{1+y}$ (y = 0, 0.1, 0.3, 0.5), (b) The inverse of magnetic susceptibility H/M vs. T for $Fe_2V_{0.9}Mn_{0.1}Al_{1+y}$ (y = 0, 0.1, 0.3, 0.5). The green dotted line shows the fitting to the Curie-Weiss function, (c, d) The magnetization M vs. B curves for $Fe_2V_{0.9}Mn_{0.1}Al_{1+y}$ (y = 0, 0.1, 0.3, 0.5) at 2.0 K and 300 K.

Table S6. Obtained results from Curie-Weiss function $H/M = (T - \theta)/ C$ for the $Fe_2V_{0.9}Mn_{0.1}Al_{1+y}$ samples.

Samples	C (K emu/mol)	μ_{eff} (μ_B/atoms)	θ (K)
$y = 0$	4.05	2.87	50
$y = 0.1$	2.02	1.95	-82.8
$y = 0.3$	1.75	1.62	-174.7
$y = 0.5$	0.68	1.12	-160.9

The *M-B* curves in Figs. S5(c) and (d), the excess Al causes a quick suppression in the magnetic susceptibility, as seen in Fig. 11(a). Our results exhibit that the magnetization decreases with increasing Mn/Al concentration. Thereby it is indicated that the addition of free carriers is weakening the itinerant-electron magnetization. More precisely, free carriers can disrupt the exchange interactions between itinerant electrons responsible for ferromagnetism/superparamagnetism. This weakens the coupling between the magnetic moments and reduces the overall magnetization.

Magnetism can play a role in enhancing the Seebeck coefficient; specific examples are magnon drag, spin fluctuations, paramagnon drag, and spin entropy. The magnetization data presented here in the case of Mn-doped Fe_2VAl indicate that the magnetic interaction is rapidly weakened by extra Al doping, while the Seebeck coefficient is enhanced above $y = 0.1$ till $y = 0.5$, as seen in Fig. 5(b). Thus, the origin of this enhancement cannot be simply attributed to the magnetic state of this sample series but is likely due to other mechanisms. For example, changes in the band structure of Al-rich Mn-doped Fe_2VAl, such as the introduction of impurity bands or modifications to existing ones due to extra Al, can impact the density of states around the Fermi level and alter the Seebeck coefficient. Another prospect is enhanced scattering of electrons due to defects or impurities can also affect the mobility of charge carriers and influence the Seebeck coefficient.

Fig. S6. The dM/dT vs. T (a) for $Fe_2V_{1-x}Mn_xAl$ (x = 0, 0.1,0.2 and 0.4) (b) for $Fe_2V_{0.9}Mn_{0.1}Al_{1+y}$ (y = 0, 0.1, 0.3, 0.5).

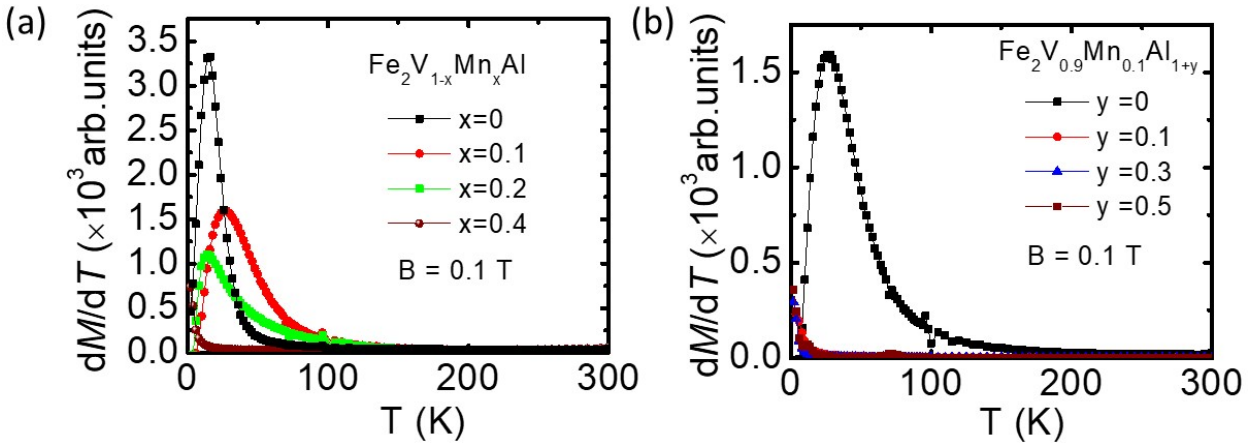

Fig.S7. Magnetic field dependent Hall resistivity of $Fe_2V_{1-x}Mn_xAl$ (a) and $Fe_2V_{0.9}Mn_{0.1}Al_{1+y}$ (b) taken at 300 K.

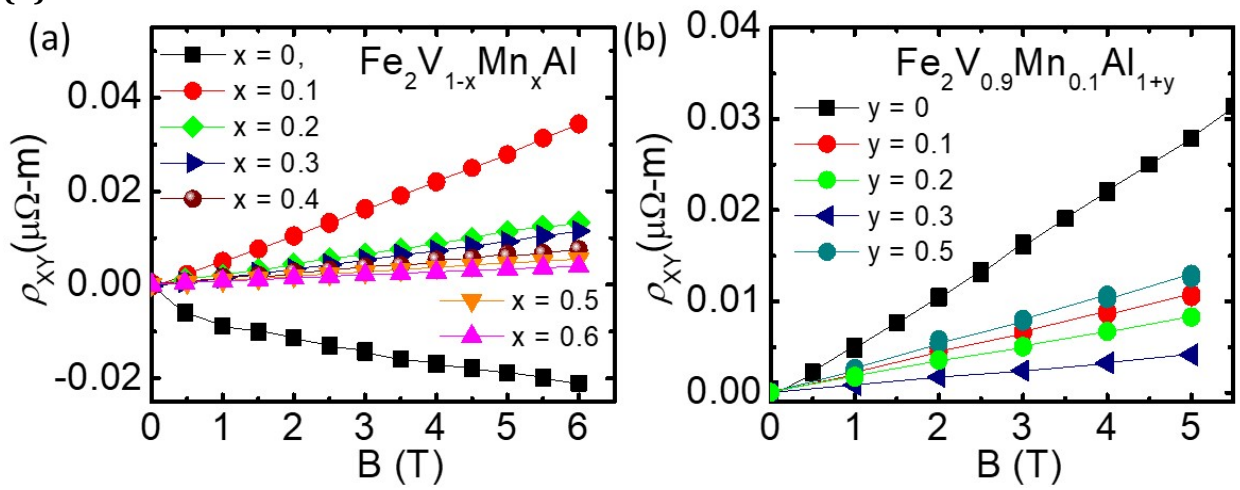

Fig.S8. Comparison of Mn substitution at the V and at the Fe site. The former yields a semimetallic ground state with the Fermi energy being located inside the valence band edge, whereas the latter results in a completely metallic density of states with a large DOS at E_F.

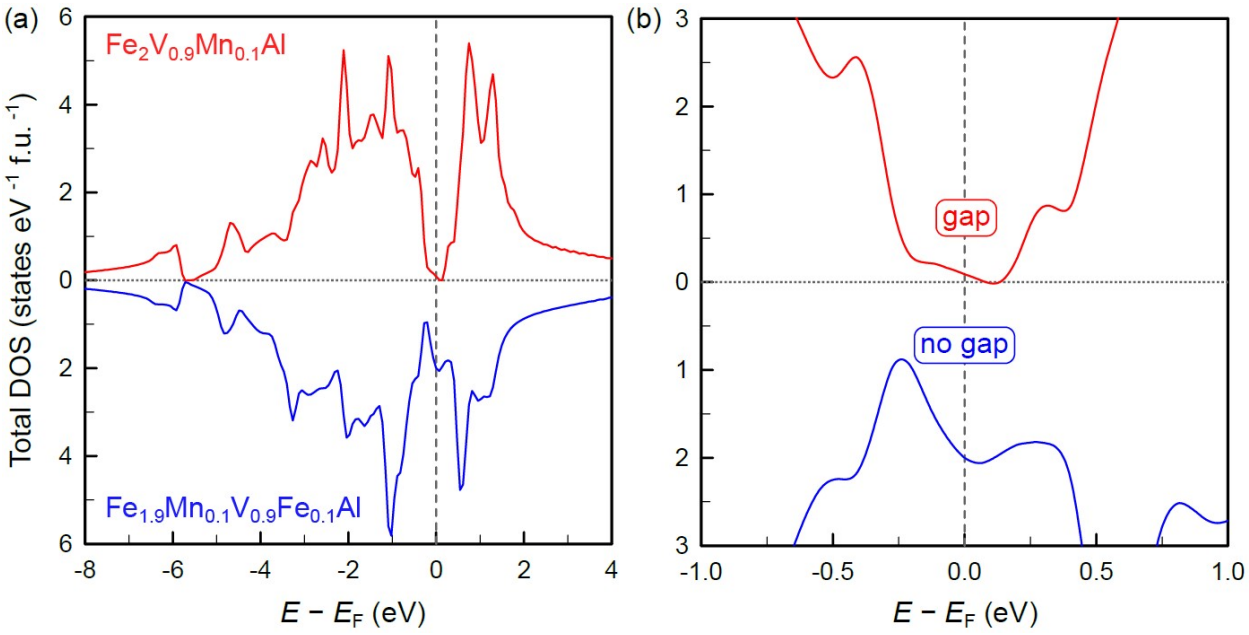

Seebeck effective mass calculation:

The experimentally obtained Seebeck coefficient and an estimate of the free electron or hole concentration from the Hall effect is presented in [Snyder et al., Adv. Funct. Mater. **32**, 2112772 (2022)]

$$\frac{m_S^*}{m^*} = 0.924\left(\frac{300K}{T}\right)\left(\frac{p}{10^{20}cm^{-3}}\right)^{2/3}\left[\frac{3\left(exp\left[\frac{|S|}{k_B/e}-2\right]-0.17\right)^{2/3}}{1+exp\left[-5\left(\frac{|S|}{k_B/e}-\frac{k_B/e}{|S|}\right)\right]}+\frac{\frac{|S|}{k_B/e}}{1+exp\left[5\left(\frac{|S|}{k_B/e}-\frac{k_B/e}{|S|}\right)\right]}\right]$$

--------(Equ.S1)

$$g(E) = \frac{8\pi\sqrt{2}}{h^3}m_{DOS}^{*3/2}\sqrt{E}$$

--------(Equ.S2)

here m_S^* is the Seebeck effective mass and m_0 is the effective mass of charrier (electron or hole), p is the hole carrier concentration measured by the Hall effect ($p = \frac{1}{eR_H}$, R_H is Hall resistance) in 10^{20} cm^{-3}, T is the absolute temperature in K, S is the Seebeck coefficient, and $k_B/e = 86.3$ μV K^{-1}. This estimate of the effective mass can support the understanding and engineering of the electronic structure as it is basically independent of scattering and the effects of microstructure (grain boundary resistance). This method is mainly helpful in describing thermoelectric materials. We estimated Seebeck effective mass by using equations S1 only if $|S| > 20$ μV K^{-1}. We found uncertainly high values of m_s^*/m^* for $|S| < 20$ μV K^{-1}.

Calculations of exchange interactions

We have calculated the exchange interactions between Mn (Fe atoms) in similar way as it was done previously for Ru_2(Fe,Mn)Ga Heusler alloys [Khmelevskyi et al., Physical Review B **91**, 094432 (2015)]. To this end we employed the first-principles magnetic force theorem (MFT) based on the Green function formalism [Liechtenstein et al., J. Magn. Magn. Mater. **67**, 65 (1987)] implemented in [Ruban et al., Physical Review B **91**, 094432 (2015)] to calculate the exchange constants of the classical Heisenberg Hamiltonian:

$$H_{cl} = -\sum_{i,j} J_{ij} \vec{e}_i \vec{e}_j , \quad (1)$$

where $\vec{e}_i$ is a directional unit vector of the magnetic spin moment at the i^{th} lattice site.

The strong localized magnetic moments appear on Mn and Fe substituted on V sites.

The calculated J_{ij} values are given in the Table S7. The positive sign of the J_{ij} is FM interaction and negative is AFM (see equ.1).

Table S7. Calculated exchange interactions

x (Mn)	J_{ij} (1NN), mRy	J_{ij} (2NN), mRy	J_{ij} (3NN), mRy
0.1	-0.32	-0.19	0.00
0.2	-0.29	-0.17	0.00
0.3	-0.27	-0.15	+0.01
0.4	-0.25	-0.14	+0.01
0.5	-0.24	-0.13	-0.01
0.6	-0.24	-0.13	+0.01

Fe-Fe interactions in $Fe_{1.9}Mn_{0.1}V_{0.9}Fe_{0.1}Al$	+0.26	-0.32	-0.02